

Asynchronous mass inversion enriched quantum anomalous Hall states in multilayer graphene

Xilin Feng,^{1,*} Zi-Ting Sun,^{1,*} and K. T. Law^{1,†}

¹*Department of Physics, Hong Kong University of Science and Technology, Clear Water Bay, Hong Kong, China*
(Dated: February 20, 2025)

Recently, multilayer graphene systems have attracted significant attention due to the discovery of a variety of intriguing phases, particularly quantum anomalous Hall (QAH) states. In rhombohedral pentalayer graphene, both $C = -5$ and $C = -3$ QAH states have been observed. While the $C = -5$ QAH state is well understood, the origin of the $C = -3$ QAH state remains unclear. In this letter, we propose that the $C = -3$ QAH state in rhombohedral pentalayer graphene (RPG) arises from an asynchronous mass inversion mechanism, driven by the interplay between trigonal warping and staggered layer order under an applied displacement field. Trigonal warping splits the low-energy bands into a central touching point and three “leg” Dirac cones. In the presence of staggered layer order, this splitting enables mass inversions driven by the displacement field to occur asynchronously at the central touching point and the “leg” Dirac cones, potentially leading to the formation of the $C = -3$ QAH state. Furthermore, this mechanism can also be applied to Bernal multilayer graphene systems, predicting the existence of additional QAH states beyond $C = \pm N, \pm 2N$ for N -layer graphene.

Introduction.—Rhombohedral multilayer graphene (RMG) has become a focal point in condensed matter physics, attracting significant attention both theoretically and experimentally. It serves as an ideal platform for investigating a variety of intriguing phases, including unconventional superconductivity [1–16], integer and fractional quantum anomalous Hall (QAH) states [17–44], ferro-valleytricity order [45, 46], and so on. Recently, both $C = -5$ and $C = -3$ QAH states have been observed in rhombohedral pentalayer graphene (RPG) [21]. The emergence of the $C = -5$ QAH state can be understood through mass inversion in a single valley with a single spin, considering the presence of layer-antiferromagnetic (LAF) order and the displacement field in a generalized Dirac model with k^5 dispersion [21, 25, 47, 48]. However, the origin of the $C = -3$ QAH state remains a puzzle until now.

In this letter, we propose an asynchronous mass inversion mechanism to explain the emergence of $C = -3$ QAH state in RPG. As discussed in previous works [17, 47, 49–53], the low-energy bands near two valleys (K and K') for RPG are primarily contributed by the B sublattice of the top layer and the A sublattice of the bottom layer, both of which are non-dimerized. The side view and hopping parameters for RPG are shown in Fig. 1 (a). In the presence of trigonal warping, the low-energy bands of RPG near the K (or K') valley split into three “leg” Dirac cones with C_3 symmetry, along with a central point exhibiting quadratic band-touching, as shown in Fig. 1 (b). Additionally, by analogy to the LAF order [51, 54–62], we introduce a staggered layer order [63], where in even-layer graphene, the charge densities between adjacent layers are oppositely polarized, and in odd-layer graphene, the middle layer lacks an order parameter, while adjacent layers on either side of the middle layer exhibit oppositely polarized charge densities. This order can be induced by Coulomb interaction near charge neutrality [51, 61, 64–70]. The coexistence of staggered layer order and the displacement field results in a momentum-dependent effective mass in the low-energy two-band model for RPG. With a fixed amplitude of

staggered layer order, the central band-touching point and the “leg” Dirac cones, having different momenta, will exhibit different effective masses under the same displacement field. Consequently, mass inversion for these two types of band-touching points will occur asynchronously at different displacement fields. When mass inversion occurs at the three “leg” Dirac cones, the change in the Chern number of RPG can be ± 3 , as each “leg” Dirac cone carries a Berry phase of $\zeta\pi$ ($\zeta = \pm 1$, corresponding to the K and K' valleys). This mechanism may give rise to a QAH state with $C = -3$ in RPG. As the displacement field increases further, mass inversion occurs at the central touching point. Due to the quadratic band-touching, this point has a Berry phase of $2\zeta\pi$. Therefore, mass inversion at this point results in a change in the Chern number of ± 2 , which could drive a topological phase transition from the QAH state with $C = -3$ to $C = -5$. Furthermore, this mechanism can also be applied to the Bernal multilayer graphene (BMG) system. Our theory solves the long-standing problem of $C = -3$ QAH state in RPG, and provides a minimal model to understand the $C \neq \pm N, \pm 2N$ QAH states in N -layer graphene for future experiments.

The low-energy two-band model for RPG—We start by introducing the low-energy two-band effective model for RPG in the presence of staggered layer order and a displacement field. The specific form of the Hamiltonian for the staggered layer order, expressed in the basis $\psi = (A_1, B_1, A_2, B_2, \dots, A_5, B_5)$, is given by:

$$H_m = m \text{Diag}(U_1, U_2, O, -U_4, -U_5), \quad (1)$$

where $U_l = (-1)^{l-1}\sigma_0$, with σ_0 being the two-dimensional identity matrix. l is the layer index, and O is the two-dimensional zero matrix. $\text{Diag}(\dots)$ denotes a diagonal matrix whose diagonal elements are listed in the brackets, and m is the amplitude of this order.

By performing perturbation theory, the Hamiltonian of the low-energy two-band model for RPG under the basis (A_1, B_5) is written as (see Supplemental Material for details):

$$H = \begin{pmatrix} M_{5,eff}(k) & X_5(\mathbf{k}) \\ X_5^\dagger(\mathbf{k}) & -M_{5,eff}(k) \end{pmatrix}, \quad (2)$$

* These two authors contributed equally to this work.

† phlaw@ust.hk

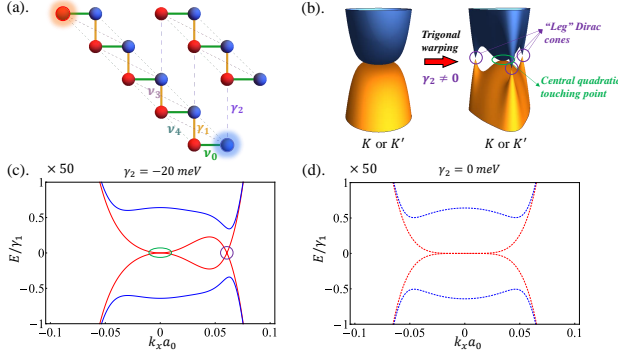


FIG. 1. (a). Side view of the rhombohedral pentalayer graphene (RPG), the blue and red atoms represent the A and B sublattices, respectively. The hopping parameters are labeled by different colors ($v_i = \sqrt{3}\gamma_i/2$): $\gamma_0 = 3160$ meV, $\gamma_1 = 390$ meV, $\gamma_2 = -20$ meV, $\gamma_3 = 315$ meV, and $\gamma_4 = 44$ meV. (b). The band structure near K (or K') valley without (left) and with (right) trigonal warping. The presence of trigonal warping leads to the low-energy bands of RPG split into three “leg” Dirac cones and a central point with quadratic band-touching. (c). The band structure of the low-energy two-band model in Eq. (2) along $k_y = 0$ line at K valley. The red solid lines represent the bands for the case where $m = 0$, $\Delta = 0$, and $\gamma_2 = -20$ meV, while the blue solid lines represent the bands in the case where $m = -10$ meV, $\Delta = 5$ meV and $\gamma_2 = -20$ meV. (d). The band structure of the low-energy two-band model in Eq. (2) along $k_y = 0$ line at K valley when the trigonal warping effect is absent ($\gamma_2 = 0$). In (c) and (d), the same color of the bands indicates the same values of m and Δ .

where $X_5(\mathbf{k})$ is the effective hopping between A_1 and B_5 , its specific form is written as:

$$X_5(\mathbf{k}) = \frac{v_0^5}{\gamma_1^4} (a_0 \xi_{\mathbf{k}}^\dagger)^5 + \frac{3v_0^2}{\gamma_1^2} (a_0 \xi_{\mathbf{k}}^\dagger)^2 \left(\frac{\gamma_2}{2} \right). \quad (3)$$

In this equation, $\xi_{\mathbf{k}} = \zeta k_x + i k_y$ ($\zeta = \pm$ for K and K' valley), a_0 is the lattice constant of graphene, v_0 represents the intralayer hopping, γ_1 represents the hopping between dimerized atoms belonging to adjacent layers, and γ_2 represents the next-nearest interlayer hopping. The band structures of the low-energy effective model with ($\gamma_2 \neq 0$) and without ($\gamma_2 = 0$) the trigonal warping effect along $k_y = 0$ line are shown in Fig 1 (c) and (d), respectively.

Additionally, the effective mass $M_{5,eff}(k)$ of the two-band model for RPG is given by:

$$M_{5,eff}(k) = (m + \Delta) - \frac{(2m - \Delta)v_0^2 a_0^2 k^2}{2\gamma_1^2}, \quad (4)$$

where m is the amplitude of the staggered layer order, Δ is the interlayer potential induced by the displacement field, and k is the amplitude of the momentum measured from the K (or K') point of the Brillouin zone (BZ).

Quantum anomalous Hall states in RPG—The effective mass given in Eq. (4) is momentum-dependent. At the central point of K or K' valley, the effective mass is expressed as $m + \Delta$. It changes sign when the displacement field satisfies $\Delta = \Delta_1 = -m$ (assuming $m < 0$). At the point with

$k \neq 0$, the effective mass changes sign at $\Delta = \Delta_2 = \frac{2\lambda-1}{1+\lambda}m$, where $\lambda = \frac{v_0^2 a_0^2 k^2}{2\gamma_1^2}$. When λ satisfies the condition $\lambda < \frac{1}{2}$, it follows that $0 < \Delta_2 < \Delta_1$. As the displacement field increases, the effective mass of the three “leg” Dirac cones changes sign first at $\Delta = \Delta_2$, followed by the sign change of the effective mass at the central quadratic touching point at $\Delta = \Delta_1$. The evolution of the band structure with increasing interlayer potential for K' valley is shown in Fig. 2 (a). To explain the appearance of the QAH state with $C = -3$, we consider staggered layer orders with amplitudes m_1 , $-m_1$, m_2 , and $-m_2$ for the four flavors $K \uparrow$, $K \downarrow$, $K' \uparrow$, and $K' \downarrow$, respectively, where $m_1 \ll m_2 < 0$. When the interlayer potential satisfies $\Delta = \Delta_2$, a mass inversion occurs at the “leg” Dirac cones, causing the Chern number of the valence band with spin-up in the K' valley (flavor $K' \uparrow$) to change from $\frac{5}{2}$ to $-\frac{1}{2}$. Meanwhile, the Chern numbers for the valence band with the other three flavors— $K \uparrow$, $K \downarrow$, and $K' \downarrow$ —are $-\frac{5}{2}$, $\frac{5}{2}$, and $-\frac{5}{2}$, respectively, and remain unchanged. Thus, the QAH state with $C = -3$ appears. When the interlayer potential further increases beyond $\Delta_1 = -m_2$, the effective mass at the central band-touching point for the $K' \uparrow$ flavor changes, leading to the emergence of a QAH state with $C = -5$.

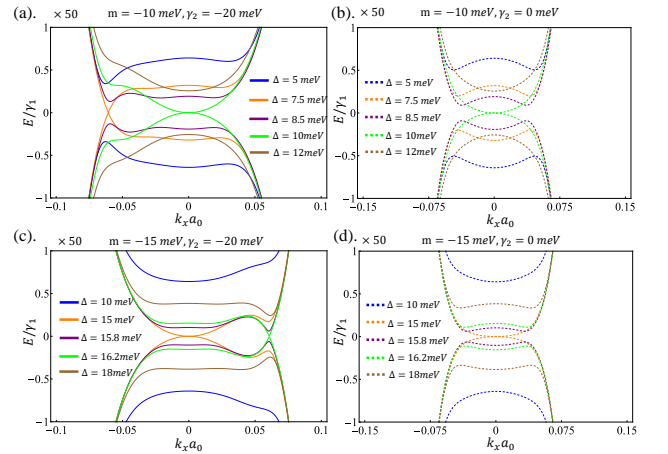


FIG. 2. (a). The evolution of the band structure for the low-energy two-band model Eq. (2) along $k_y = 0$ line with increasing interlayer potential at K' valley, in the presence of staggered layer order Eq. (1), is shown, where the parameters are $v_0 = \frac{\sqrt{3}}{2} \times 3160$ meV, $\gamma_1 = 390$ meV, $m = m_2 = -10$ meV and $\gamma_2 = -20$ meV. (b). The evolution of the band structure with increasing interlayer potential in the case where $\gamma_2 = 0$ (without trigonal warping). All other parameters are the same as in (a). (c). The evolution of the band structure with increasing interlayer potential at K valley, in the presence of the staggered sublattice order given in Eq. (5). The parameters are $m = m_1 = -15$ meV and $\gamma_2 = -20$ meV. (d). The evolution of the band structure with increasing interlayer potential in the case where $\gamma_2 = 0$. All other parameters are the same as in (c).

For contrast, we also show the evolution of the band structure with increasing interlayer potential in the case where $\gamma_2 = 0$ (without trigonal warping) in Fig. 2 (b). As the interlayer potential increases, the effective mass at the central point of K' valley will change sign at $\Delta = \Delta_1 = -m_2$, with

no other gap-closing occurring. Additionally, the dispersion of the band-touching point follows the form k^5 . Therefore, in the absence of trigonal warping, increasing the interlayer potential induces a single topological phase transition from the $C = 0$ state to a QAH state with $C = -5$. In addition, if there is no staggered layer order ($m = 0$), although this effective mass (Eq. 4) remains momentum-dependent, its sign is only determined by the sign of the interlayer potential Δ at both $k = 0$ and $k \neq 0$ points. Therefore, increasing the interlayer potential (from negative to positive) will induce mass inversion at both the central point and the “leg” Dirac cones simultaneously.

The entire phase diagram under increasing displacement field for RPG—Using the staggered layer order defined in Eq. (1), we can explain the topological phase transitions from the $C = 0$ state to the $C = -3$ QAH state, and then to the $C = -5$ QAH state. However, as the displacement field continues to increase, the transition from the $C = -5$ to the $C = -3$ QAH state, and then to the $C = 0$ state, remains unexplained. To account for this sequence of topological phase transitions, it is necessary to introduce an order parameter that first induces mass inversion at the central point. One natural choice is the staggered sublattice order, which describes a uniform charge density across each layer but with opposite polarizations between the A and B sublattices within a single layer. This order also satisfies the charge neutrality condition. The specific form of the Hamiltonian for this order parameter in the basis $\psi = (A_1, B_1, A_2, B_2, \dots, A_5, B_5)$ is written as:

$$H'_m = m \text{Diag}(\sigma_z, \sigma_z, \dots, \sigma_z), \quad (5)$$

where σ_z is the Pauli matrix of the sublattice degree of freedom on each layer. By performing the perturbation theory, the effective mass for the low-energy effective model is derived as:

$$M'_{5,eff}(k) = (m + \Delta) + \frac{(2m + \Delta)v_0^2 k^2}{2\gamma_1^2}. \quad (6)$$

The hopping term for the low-energy two-band model is the same as Eq.(3). For $k = 0$ point, the effective mass changes sign at $\Delta = \Delta'_1 = -m$ (assuming $\Delta > 0$ and $m < 0$). However, for $k \neq 0$ points, unlike the case of the staggered layer order in Eq. (1), the effective mass changes sign at $\Delta = \Delta'_2 = -m \frac{1+2\lambda}{1+\lambda}$ which is larger than $\Delta'_1 = -m$ due to $\lambda = \frac{v_0^2 a_0^2 k^2}{2\gamma_1^2} > 0$. Thus, as the displacement field increases, the effective mass at the central point of the K (or K') valley changes sign first at $\Delta = \Delta'_1 = -m$, followed by the sign change of the effective mass of the three “leg” Dirac cones at $\Delta = \Delta'_2 > \Delta'_1$. In the presence of the staggered sublattice order, the evolution of the band structure at the K valley with increasing interlayer potential is shown in Fig. 2 (c) and (d), for cases with and without trigonal warping, respectively.

We then assume that the staggered orders for the four flavors $K \uparrow$, $K \downarrow$, $K' \uparrow$, and $K' \downarrow$ are given as H'_{m_1} , $-H'_{m_1}$, H_{m_2} , and $-H_{m_2}$, respectively, with $0 > m_2 > m_1$. When the interlayer potential satisfies $0 < \Delta < -m_2$, as Δ increases, a mass inversion happens at the three “leg” Dirac cones for $K' \uparrow$ flavor, causing the Chern number of RPG to change from $C = 0$

to $C = -3$. Then, when $\Delta = -m_2$, the effective mass at the central band-touching point for electrons with flavor $K' \uparrow$ changes sign, leading to a further change in the Chern number from $C = -3$ to $C = -5$. When the displacement field satisfies $-m_2 < \Delta < -m_1$, since $m_2 > m_1$, the Chern number for RPG remains $C = -5$. As the displacement field continues to increase, for electrons with flavor $K \uparrow$, the effective mass of the central band-touching point changes sign at $\Delta = -m_1$, leading to a topological phase transition from the QAH state with $C = -5$ to $C = -3$. With further increases in the displacement field, the effective masses of the three “leg” Dirac cones with flavor $K \uparrow$ change sign, resulting in a topological phase transition from the QAH state with $C = -3$ to the state with $C = 0$. Consequently, we deduce that as the displacement field increases, the Chern number for RPG evolves as $0 \rightarrow -3 \rightarrow -5 \rightarrow -3 \rightarrow 0$, which is consistent with experimental observations [21]. Moreover, within this mechanism, we can deduce that at $\Delta = 0$, the $C = 0$ state in RPG corresponds to a state where both the spin and valley Chern numbers are 0. When the displacement field becomes sufficiently large, although the total Chern number of RPG remains 0, the system transitions into a quantum valley Hall state with a valley Chern number of 5. Additionally, to make the analysis more practical, we investigate the band structure and topological phase transition using the full Hamiltonian of RPG, taking into account the staggered layer (or sublattice) order and displacement field. The asynchronous mass inversion at the central touching point and “leg” Dirac cones remains unchanged (see Supplemental Material for details). Therefore, the low-energy effective model in Eq. (2) captures the key physical mechanism underlying the QAH states in RPG.

The low-energy effective model for BMG—Next, we apply this asynchronous mass inversion mechanism to explore the possible enriched QAH states in BMG. For N -layer BMG, similar to the case of RMG, the combination of trigonal warping and staggered layer order also gives rise to additional QAH states with Chern number $C \neq \pm N, \pm 2N$ when a displacement field is applied. However, unlike the case in RMG, the low-energy effective model for BMG is no longer a two-band model. For Bernal N -layer graphene, if N is even, the Hamiltonian can be decomposed into $N/2$ mutually coupled bilayer graphene systems [71]. We can then project the Hamiltonian for each bilayer graphene onto the basis which is composed of non-dimerized “atoms” to obtain an N -dimensional low-energy effective model (see Supplemental Material for details). If N is odd, the low-energy effective model for BMG consists of $N/2$ mutually coupled bilayer graphene systems along with an additional monolayer graphene that couples to these bilayer graphenes. The presence of this additional monolayer graphene results in a metallic state, even when staggered layer orders are considered [63], thereby preventing the formation of a QAH state. As a result, this paper focuses on even-layer BMGs. Specifically, we use Bernal tetralayer graphene (BTG) as an example in the following discussion. The side view and hopping parameters for BTG are shown in Fig. 3 (a), and the staggered layer order is written as:

$$H_m^B = m \text{Diag}(U_1, U_2, U_3, U_4), \quad (7)$$

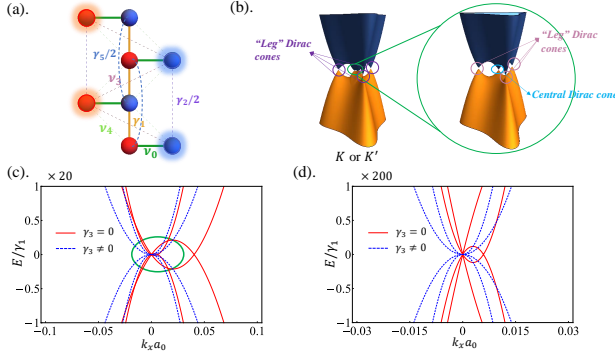


FIG. 3. (a). Side view of the Bernal tetralayer graphene (BTG), the blue and red atoms represent the A and B sublattices, respectively. The hopping parameters are indicated by different colors ($v_i = \frac{\sqrt{3}}{2}\gamma_i$): $\gamma_0 = 3000$ meV, $\gamma_1 = 400$ meV, $\gamma_2 = -20$ meV, $\gamma_3 = 300$ meV, and $\gamma_4 = \gamma_5 = 40$ meV. Here, the displacement field and staggered layer orders are set to zero: $\Delta = 0$, and $m = 0$. (b). The band structure near K (or K') valley in the presence of the trigonal warping. The bands in the green circle show the enlarged view near K (or K') point. (c). The band structure for the low-energy effective model along $k_y = 0$ line with and without γ_3 , which are shown by red solid and blue dashed lines, respectively. Here, we set $\Delta = 0$ and $m = 0$. (d). Enlarged view of the band structure for the region marked by the green circle in (c).

where $U_l = (-1)^{l-1}\sigma_0$, with l labeling the layer index. Then the low-energy effective model for BTG can be derived as:

$$H = \begin{pmatrix} h_{eff}(\lambda_1) + h_{\Delta}(s_{1,1}, t_{1,1}) & h_c(s_{1,3}, t_{1,3}) \\ h_c(s_{1,3}, t_{1,3}) & h_{eff}(\lambda_3) + h_{\Delta}(s_{3,3}, t_{3,3}) \end{pmatrix}, \quad (8)$$

where

$$h_{eff}(\lambda) = \begin{pmatrix} 0 & \lambda v_3 \xi_{\mathbf{k}} - \frac{1}{\lambda \gamma_1} v_0^2 (\xi_{\mathbf{k}}^{\dagger})^2 \\ \lambda v_3 \xi_{\mathbf{k}}^{\dagger} - \frac{1}{\lambda \gamma_1} v_0^2 (\xi_{\mathbf{k}})^2 & 0 \end{pmatrix}, \quad (9)$$

$h_{\Delta}(s, t) = \begin{pmatrix} s\Delta + m & 0 \\ 0 & t\Delta - m \end{pmatrix}$, and $h_c(s, t) = \begin{pmatrix} s\Delta & 0 \\ 0 & t\Delta \end{pmatrix}$. The parameters in Eq. (8) can be found in Supplemental Material. The band structure near K (or K') for the low-energy effective model of BTG with trigonal warping is shown in Fig. 3 (b). Here, the displacement field and staggered layer order are set to zero: $\Delta = 0$ and $m = 0$.

Topological phase transitions in Bernal tetralayer graphene—The Hamiltonian in Eq. (8) can be interpreted as two coupled bilayer graphenes with different hopping parameters. In the following discussion, we refer to these two bilayer graphene systems as the first ($H_{eff}^1 = h_{eff}(\lambda_1) + h_{\Delta}(s_{1,1}, t_{1,1})$) and the second ($H_{eff}^2 = h_{eff}(\lambda_3) + h_{\Delta}(s_{3,3}, t_{3,3})$) bilayer graphene, respectively. Due to trigonal warping, the energy bands of both first and second bilayer graphene split into one central Dirac cone and three “leg” Dirac cones at the K and K' valleys. In both bilayer graphenes, the central Dirac cone and the “leg” Dirac cone possess Berry phases of $-\zeta\pi$ and $\zeta\pi$, respectively, where $\zeta = \pm$ corresponds to the K and K' valleys. Furthermore, although the central Dirac cones of

these two bilayer graphenes overlap at the K (or K') point, the momentum amplitudes k of the three “leg” Dirac cones differ between these two systems, as shown in Fig. 3 (b). Specifically, since $\lambda_3 > \lambda_1$, the momentum amplitude of the three “leg” Dirac cones in the second bilayer graphene (k_2) is larger than that in the first bilayer graphene (k_1). To highlight the effect of trigonal warping more clearly, the band structures along the $k_y = 0$ line for BTG with $\Delta = 0$ and $m = 0$ are shown in Fig. 3 (c) and (d). Additionally, as shown in the low-energy effective model (Eq. (8)), the coupling strength between two bilayer graphenes is determined by the displacement field. For a fixed staggered layer order, the evolution of the band structure for the low-energy effective model of BTG with the increasing displacement field is illustrated in Fig. 4 (a). The coupling between these two bilayer graphenes opens the gap at band-touching points and lowers the energy of the band near the central point of the K (or K') valley, leading to a topological phase transition through a mass-inversion process. If mass inversion occurs in the bands belonging to the first bilayer graphene, the small momentum amplitude of the three “leg” Dirac cones causes the effective masses of both the central Dirac cone and the three “leg” Dirac cones to change sign simultaneously. In contrast, if mass inversion occurs in the bands belonging to the second bilayer graphene, only the effective mass of the central Dirac cone will change sign, as the three “leg” Dirac cones are located far from the central point of the K (or K') valley.

On the other hand, based on the effective masses of the first and second bilayer graphenes, we conclude that for $m > 0$, when the interlayer potential satisfies $-3m < \Delta < 0$, the amplitude of the effective mass for the first bilayer graphene, $M_1 = |s_{1,1}\Delta + m|$, is smaller than that for the second bilayer graphene, $M_2 = |s_{3,3}\Delta + m|$, i.e., $M_1 < M_2$. As a result, the energy gap between the valence and conduction bands in the first bilayer graphene is smaller than that in the second bilayer graphene. Conversely, for $\Delta > 0$, since $M_1 > M_2$, the energy gap in the second bilayer graphene becomes smaller than that in the first bilayer graphene. The band structures corresponding to these two bilayer graphenes are shown in Fig. 4 (b). Therefore, for $m > 0$, when $-3m < \Delta < 0$, the topological phase transition results from mass inversion in the first bilayer graphene, which changes the sign of the effective mass at both the central Dirac cone and the three “leg” Dirac cones, causing the Chern number of the low-energy band to change by ± 2 . When $\Delta > 0$, the phase transition arises from mass inversion in the second bilayer graphene, which only changes the sign of the effective mass at the central Dirac cone, leading to a change in the Chern number by ± 1 . For the case $m < 0$, a similar result can be obtained: when $\Delta < 0$ or $\Delta > -3m$, $M_1 > M_2$; while for $0 < \Delta < -3m$, $M_1 < M_2$.

Quantum anomalous Hall states in BTG—In analogy to the case in RPG, to investigate the QAH states in BTG, we assume that the staggered orders for the four flavors $K \uparrow$, $K \downarrow$, $K' \uparrow$, and $K' \downarrow$ are given by H_m^B , H_m^B , H_{-m}^B , and H_{-m}^B , respectively, with $m > 0$. When $\Delta > 3m$, the total Chern number in the K valley for each spin is 3, while in the K' valley for each spin it is 0, resulting in a QAH state in BTG with

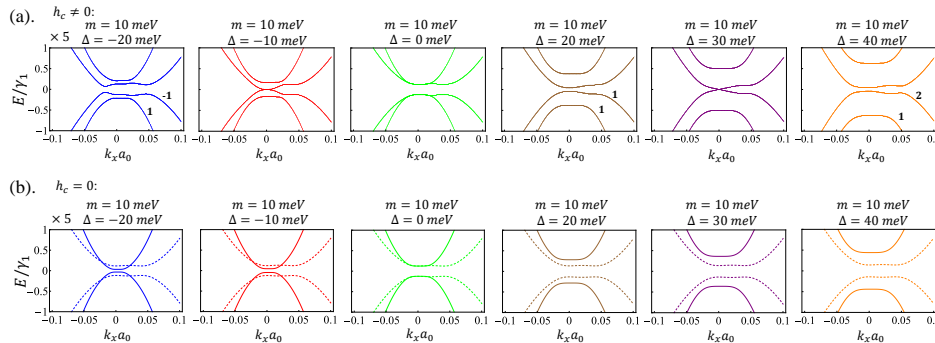


FIG. 4. (a). The evolution of the band structure for the low-energy effective model of Bernal tetralayer graphene (BTG) with the increasing displacement field in K valley. The Chern number for each valence band is indicated near the respective band. The parameters are $v_0 = \frac{\sqrt{3}}{2} \times 3000 \text{ meV}$, $\gamma_1 = 400 \text{ meV}$, $v_3 = \frac{\sqrt{3}}{2} \times 300 \text{ meV}$, and $m = 10 \text{ meV}$. (b). The evolution of the band structure for the low-energy effective model of BTG with increasing displacement field, in the absence of inter-bilayer coupling ($h_c = 0$). The solid and dashed lines represent the bands of the first and the second bilayer graphenes, respectively.

a total Chern number of $C = 6$. It is worth noting that for BTG, the topological phase transition behavior remains the same whether we consider the staggered layer or sublattice order. This is because the low-energy bands for BTG near the K and K' points are primarily contributed by the sublattices (A_1, B_2, A_3, B_4). When projecting the staggered layer and sublattice orders onto the basis formed by these sublattices, they yield the same expressions, leading to identical phase diagrams as the displacement field increases. Additionally, by using the full Hamiltonian of BTG [65, 72], we investigate the topological phase transitions. While the band structure differs from that of the low-energy effective model, the QAH state with a total Chern number $C = 6$ persists (see Supplemental Material for details). Therefore, the low-energy effective model (Eq. (8)) provides a good description for the topological properties of the BTG.

Conclusion and Discussion—In summary, we propose that for rhombohedral N -layer graphene, the emergence of QAH states with a Chern number $C \neq \pm N, \pm 2N$ can be attributed to an asynchronous mass inversion mechanism, which arises from the interplay between trigonal warping and staggered layer (or sublattice) order under a displacement field. The trigonal warping effect splits the low-energy bands of this multi-layer graphene into the central touching point and “leg” Dirac cones in the K (or K') valley. By incorporating the presence of staggered layer (or sublattice) order and increasing displacement fields, mass inversion can occur asynchronously for the

central touching point and the “leg” Dirac cones, leading to a change in the Chern number that is not necessarily $\pm N$. Within this mechanism, we explain the appearance of the $C = -3$ QAH state in RPG which is not clear so far [21]. In addition, the topological phase transition observed in RPG with the increasing displacement field can be explained by assuming spin-polarized staggered sublattice and layer orders in the K and K' valleys, respectively. Furthermore, under this assumption, as the displacement field increases from zero to sufficiently large values, the system transitions from a state with both spin and valley Chern numbers equal to zero to a quantum valley Hall state with a valley Chern number of 5, which is experimentally detectable. Moreover, it is worth noting that in experiments [21], QAH states are observed only under the application of a small, finite magnetic field. This observation may be attributed to the stabilization of valley polarization states, which arise from the coupling between orbital magnetization [73–80] and the applied magnetic field. Interestingly, the asynchronous mass inversion mechanism can also be applied to BMG, revealing the emergence of the $C = 6$ QAH state in BTG, which can be observed in experiments.

Acknowledgements—K. T. L. acknowledges the support of the Ministry of Science and Technology, China, and Hong Kong Research Grant Council through Grants No. 2020YFA0309600, No. RFS2021-6S03, No. C6025-19G, No. AoE/P-701/20, No. 16310520, No. 16307622, and No. 16309223.

[1] H. Zhou, T. Xie, T. Taniguchi, K. Watanabe, and A. F. Young, *Nature* **598**, 434 (2021).
 [2] A. Ghazaryan, T. Holder, M. Serbyn, and E. Berg, *Physical Review Letters* **127**, 247001 (2021).
 [3] Y.-Z. You and A. Vishwanath, *Physical Review B* **105**, 134524 (2022).
 [4] H. Zhou, L. Holleis, Y. Saito, L. Cohen, W. Huynh, C. L. Patterson, F. Yang, T. Taniguchi, K. Watanabe, and A. F. Young,

Science **375**, 774 (2022).
 [5] Y.-Z. Chou, F. Wu, J. D. Sau, and S. Das Sarma, *Physical Review B* **106**, 024507 (2022).
 [6] E. Pangburn, L. Haurie, A. Crépieux, O. A. Awoga, A. M. Black-Schaffer, C. Pépin, and C. Bena, *Physical Review B* **108**, 134514 (2023).
 [7] W. Qin, C. Huang, T. Wolf, N. Wei, I. Blinov, and A. H. MacDonald, *Physical Review Letters* **130**, 146001 (2023).

- [8] G. Wagner, Y. H. Kwan, N. Bultinck, S. H. Simon, and S. Parameswaran, *Physical Review B* **110**, 214517 (2024).
- [9] C. Li, F. Xu, B. Li, J. Li, G. Li, K. Watanabe, T. Taniguchi, B. Tong, J. Shen, L. Lu, *et al.*, *Nature*, 1 (2024).
- [10] J. Yang, X. Shi, S. Ye, C. Yoon, Z. Lu, V. Kakani, T. Han, J. Seo, L. Shi, K. Watanabe, *et al.*, arXiv preprint arXiv:2408.09906 (2024).
- [11] E. Viñas Boström, A. Fischer, J. B. Profe, J. Zhang, D. M. Kennes, and A. Rubio, *npj Computational Materials* **10**, 163 (2024).
- [12] A. Fischer, L. Klebl, J. B. Profe, A. Rothstein, L. Waldecker, B. Beschoten, T. O. Wehling, and D. M. Kennes, *Physical Review Research* **6**, L012003 (2024).
- [13] M. Geier, M. Davydova, and L. Fu, arXiv preprint arXiv:2409.13829 (2024).
- [14] C. W. Chau, S. A. Chen, and K. Law, arXiv preprint arXiv:2404.19237 (2024).
- [15] Y.-Q. Wang, Z.-Q. Gao, and H. Yang, arXiv preprint arXiv:2410.05384 (2024).
- [16] S. Wang, Z. Zhang, H. Li, C. Sanborn, W. Zhao, S. Wang, K. Watanabe, T. Taniguchi, M. F. Crommie, G. Chen, *et al.*, *Nano Letters* (2024).
- [17] R. Nandkishore and L. Levitov, *Physical Review B—Condensed Matter and Materials Physics* **82**, 115124 (2010).
- [18] Y. Shi, S. Xu, Y. Yang, S. Slizovskiy, S. V. Morozov, S.-K. Son, S. Ozdemir, C. Mullan, J. Barrier, J. Yin, *et al.*, *Nature* **584**, 210 (2020).
- [19] A. Kerelsky, C. Rubio-Verdú, L. Xian, D. M. Kennes, D. Halbertal, N. Finney, L. Song, S. Turkel, L. Wang, K. Watanabe, *et al.*, *Proceedings of the National Academy of Sciences* **118**, e2017366118 (2021).
- [20] Z. Dong, A. S. Patri, and T. Senthil, *Physical Review Letters* **133**, 206502 (2024).
- [21] T. Han, Z. Lu, G. Scuri, J. Sung, J. Wang, T. Han, K. Watanabe, T. Taniguchi, H. Park, and L. Ju, *Nature Nanotechnology* **19**, 181 (2024).
- [22] T. Han, Z. Lu, Y. Yao, J. Yang, J. Seo, C. Yoon, K. Watanabe, T. Taniguchi, L. Fu, F. Zhang, *et al.*, *Science* **384**, 647 (2024).
- [23] K. Liu, J. Zheng, Y. Sha, B. Lyu, F. Li, Y. Park, Y. Ren, K. Watanabe, T. Taniguchi, J. Jia, *et al.*, *Nature nanotechnology* **19**, 188 (2024).
- [24] Y. Sha, J. Zheng, K. Liu, H. Du, K. Watanabe, T. Taniguchi, J. Jia, Z. Shi, R. Zhong, and G. Chen, *Science* **384**, 414 (2024).
- [25] Z. Liu and J. Wang, arXiv preprint arXiv:2401.13413 (2024).
- [26] J. Dong, T. Wang, T. Wang, T. Soejima, M. P. Zaletel, A. Vishwanath, and D. E. Parker, *Physical Review Letters* **133**, 206503 (2024).
- [27] T. Soejima, J. Dong, T. Wang, T. Wang, M. P. Zaletel, A. Vishwanath, and D. E. Parker, *Physical Review B* **110**, 205124 (2024).
- [28] K. Kudo, R. Nakai, and K. Nomura, *Physical Review B* **110**, 245135 (2024).
- [29] R. Perea-Causin, H. Liu, and E. J. Bergholtz, arXiv preprint arXiv:2412.02745 (2024).
- [30] M. Xie and S. Das Sarma, *Physical Review B* **109**, L241115 (2024).
- [31] Z. Lu, T. Han, Y. Yao, A. P. Reddy, J. Yang, J. Seo, K. Watanabe, T. Taniguchi, L. Fu, and L. Ju, *Nature* **626**, 759 (2024).
- [32] L. Ju, A. H. MacDonald, K. F. Mak, J. Shan, and X. Xu, *Nature Reviews Materials*, 1 (2024).
- [33] K. Huang, S. D. Sarma, and X. Li, arXiv preprint arXiv:2408.05139 (2024).
- [34] S. Das Sarma and M. Xie, *Physical Review B* **110**, 155148 (2024).
- [35] J. Herzog-Arbeitman, Y. Wang, J. Liu, P. M. Tam, Z. Qi, Y. Jia, D. K. Efetov, O. Vafek, N. Regnault, H. Weng, *et al.*, *Physical Review B* **109**, 205122 (2024).
- [36] J. Xie, Z. Huo, X. Lu, Z. Feng, Z. Zhang, W. Wang, Q. Yang, K. Watanabe, T. Taniguchi, K. Liu, *et al.*, arXiv preprint arXiv:2405.16944 (2024).
- [37] K. Huang, X. Li, S. Das Sarma, and F. Zhang, *Physical Review B* **110**, 115146 (2024).
- [38] J. An, A. C. Balram, and G. Murthy, *Physical Review B* **110**, L081103 (2024).
- [39] H. Lu, H.-Q. Wu, B.-B. Chen, K. Sun, and Z. Y. Meng, arXiv preprint arXiv:2403.03258 (2024).
- [40] B. Zhou, H. Yang, and Y.-H. Zhang, *Physical Review Letters* **133**, 206504 (2024).
- [41] S. H. Aronson, T. Han, Z. Lu, Y. Yao, K. Watanabe, T. Taniguchi, L. Ju, and R. C. Ashoori, arXiv preprint arXiv:2408.11220 (2024).
- [42] Z. Wei, A.-K. Wu, M. Gonçalves, and S.-Z. Lin, *Physical Review B* **111**, 035116 (2025).
- [43] Z. Lu, T. Han, Y. Yao, Z. Hadjri, J. Yang, J. Seo, L. Shi, S. Ye, K. Watanabe, T. Taniguchi, *et al.*, *Nature*, 1 (2025).
- [44] F. Pichler, W. Kadow, C. Kuhlenskamp, and M. Knap, *Physical Review B* **111**, 075108 (2025).
- [45] T. Han, Z. Lu, G. Scuri, J. Sung, J. Wang, T. Han, K. Watanabe, T. Taniguchi, L. Fu, H. Park, *et al.*, *Nature* **623**, 41 (2023).
- [46] M. M. Islam, S. Alam, M. R. I. Udoy, M. S. Hossain, K. E. Hamilton, and A. Aziz, *Applied Physics Reviews* **12** (2025).
- [47] F. Zhang, J. Jung, G. A. Fiete, Q. Niu, and A. H. MacDonald, *Physical review letters* **106**, 156801 (2011).
- [48] J. Jung, F. Zhang, and A. H. MacDonald, *Physical Review B—Condensed Matter and Materials Physics* **83**, 115408 (2011).
- [49] H. Min, G. Borghi, M. Polini, and A. H. MacDonald, *Physical Review B—Condensed Matter and Materials Physics* **77**, 041407 (2008).
- [50] M. Koshino and E. McCann, *Physical Review B—Condensed Matter and Materials Physics* **80**, 165409 (2009).
- [51] F. Zhang, H. Min, M. Polini, and A. MacDonald, *Physical Review B—Condensed Matter and Materials Physics* **81**, 041402 (2010).
- [52] F. Zhang, B. Sahu, H. Min, and A. H. MacDonald, *Physical Review B—Condensed Matter and Materials Physics* **82**, 035409 (2010).
- [53] R. Nandkishore and L. Levitov, *Physical review letters* **104**, 156803 (2010).
- [54] J. Nilsson, A. Castro Neto, N. Peres, and F. Guinea, *Physical Review B—Condensed Matter and Materials Physics* **73**, 214418 (2006).
- [55] Y. Lemonik, I. Aleiner, and V. Fal'ko, *Physical Review B—Condensed Matter and Materials Physics* **85**, 245451 (2012).
- [56] T. C. Lang, Z. Y. Meng, M. M. Scherer, S. Uebelacker, F. F. Assaad, A. Muramatsu, C. Honerkamp, and S. Wessel, *Physical review letters* **109**, 126402 (2012).
- [57] M. M. Scherer, S. Uebelacker, and C. Honerkamp, *Physical Review B—Condensed Matter and Materials Physics* **85**, 235408 (2012).
- [58] M. Kharitonov, *Physical Review B—Condensed Matter and Materials Physics* **86**, 195435 (2012).
- [59] Y. Wang, H. Wang, J.-H. Gao, and F.-C. Zhang, *Physical Review B—Condensed Matter and Materials Physics* **87**, 195413 (2013).
- [60] J. Yuan, D.-H. Xu, H. Wang, Y. Zhou, J.-H. Gao, and F.-C.

- Zhang, Physical Review B—Condensed Matter and Materials Physics **88**, 201109 (2013).
- [61] M. Liang, S. Li, and J.-H. Gao, Physical Review B **105**, 045419 (2022).
- [62] X.-C. Jiang, Z.-Y. Song, Z. Ruan, and Y.-Z. Zhang, Physical Review Research **6**, 013255 (2024).
- [63] A. L. Grushina, D.-K. Ki, M. Koshino, A. A. Nicolet, C. Faugeras, E. McCann, M. Potemski, and A. F. Morpurgo, Nature communications **6**, 6419 (2015).
- [64] D.-H. Xu, J. Yuan, Z.-J. Yao, Y. Zhou, J.-H. Gao, and F.-C. Zhang, Physical Review B—Condensed Matter and Materials Physics **86**, 201404 (2012).
- [65] A. Ghazaryan, T. Holder, E. Berg, and M. Serbyn, Physical Review B **107**, 104502 (2023).
- [66] J. M. Koh, J. Alicea, and É. Lantagne-Hurtubise, Physical Review B **109**, 035113 (2024).
- [67] J. M. Koh, A. Thomson, J. Alicea, and É. Lantagne-Hurtubise, Physical Review B **110**, 245118 (2024).
- [68] T. Wang, M. Vila, M. P. Zaletel, and S. Chatterjee, Physical Review Letters **132**, 116504 (2024).
- [69] Y. Zhumagulov, D. Kochan, and J. Fabian, Physical Review Letters **132**, 186401 (2024).
- [70] Y. Zhumagulov, D. Kochan, and J. Fabian, Physical Review B **110**, 045427 (2024).
- [71] M. Koshino and E. McCann, Physical Review B—Condensed Matter and Materials Physics **83**, 165443 (2011).
- [72] H. Chen, A. Arora, J. C. Song, and K. P. Loh, Nature Communications **14**, 7925 (2023).
- [73] T. Thonhauser, D. Ceresoli, D. Vanderbilt, and R. Resta, Physical review letters **95**, 137205 (2005).
- [74] D. Xiao, J. Shi, and Q. Niu, Physical review letters **95**, 137204 (2005).
- [75] D. Ceresoli, T. Thonhauser, D. Vanderbilt, and R. Resta, Physical Review B—Condensed Matter and Materials Physics **74**, 024408 (2006).
- [76] J. Shi, G. Vignale, D. Xiao, and Q. Niu, Physical review letters **99**, 197202 (2007).
- [77] D. Xiao, M.-C. Chang, and Q. Niu, Reviews of modern physics **82**, 1959 (2010).
- [78] R. Bianco and R. Resta, Physical review letters **110**, 087202 (2013).
- [79] R. Bianco and R. Resta, Physical Review B **93**, 174417 (2016).
- [80] J. Zhu, J.-J. Su, and A. H. MacDonald, Physical Review Letters **125**, 227702 (2020).

SUPPLEMENTAL MATERIAL NOTE 1: RHOMBOHEDRAL MULTILAYER GRAPHENE

A. Low-energy effective model for rhombohedral multilayer graphene

In this section, we derive the low-energy effective two-band model for rhombohedral multilayer graphene (RMG), incorporating the effects of trigonal warping, displacement field, and staggered layer order. The basis for the RMG is expressed as:

$$\psi = (A_1, B_1, A_2, B_2, \dots, A_N, B_N), \quad (\text{S1})$$

where N denotes the number of layers. Therefore, the matrix form of the Hamiltonian for RMG is written as:

$$H = \begin{pmatrix} H_0 & V & W & & & & \\ V^\dagger & H_0 & V & W & & & \\ W^\dagger & V^\dagger & H_0 & V & W & & \\ & W^\dagger & V^\dagger & H_0 & V & W & \\ & & & \ddots & \ddots & \ddots & \ddots \\ & & & & & & \ddots \end{pmatrix}, \quad (\text{S2})$$

where the intralayer hopping is expressed by $H_0 = \begin{pmatrix} 0 & v_0 \xi_{\mathbf{k}}^\dagger \\ v_0 \xi_{\mathbf{k}} & 0 \end{pmatrix}$, and $\xi_{\mathbf{k}} = \zeta k_x + i k_y$ ($\zeta = \pm 1$ representing the K and K' valley, respectively). The nearest interlayer hopping is represented by $V = \begin{pmatrix} -v_4 \xi_{\mathbf{k}}^\dagger & v_3 \xi_{\mathbf{k}} \\ \gamma_1 & -v_4 \xi_{\mathbf{k}}^\dagger \end{pmatrix}$, and the next-nearest interlayer hopping is written as $W = \begin{pmatrix} 0 & \gamma_2/2 \\ 0 & 0 \end{pmatrix}$. The side view of rhombohedral multilayer graphene and the hopping terms are labeled in Fig.S1 (a) ($v_i = \sqrt{3}\gamma_i/2$, in this figure, the pentalayer graphene is shown as an example).

The Hamiltonian for staggered layer order is expressed as:

$$H_m = \begin{cases} m \text{Diag}(U_1, \dots, U_{(N-1)/2}, O, -U_{(N+3)/2}, \dots, -U_N) & \text{if } N \in \text{odd} \\ m \text{Diag}(U_1, \dots, U_l, \dots, U_N) & \text{if } N \in \text{even} \end{cases}, \quad (\text{S3})$$

where $U_l = (-1)^{l-1} \begin{pmatrix} 1 & 0 \\ 0 & 1 \end{pmatrix}$, $O = \begin{pmatrix} 0 & 0 \\ 0 & 0 \end{pmatrix}$, l is the layer index, and m is the amplitude of this order. $\text{Diag}(\dots)$ denotes a diagonal matrix whose diagonal elements are listed in the brackets. In addition, the Hamiltonian for interlayer potential induced by

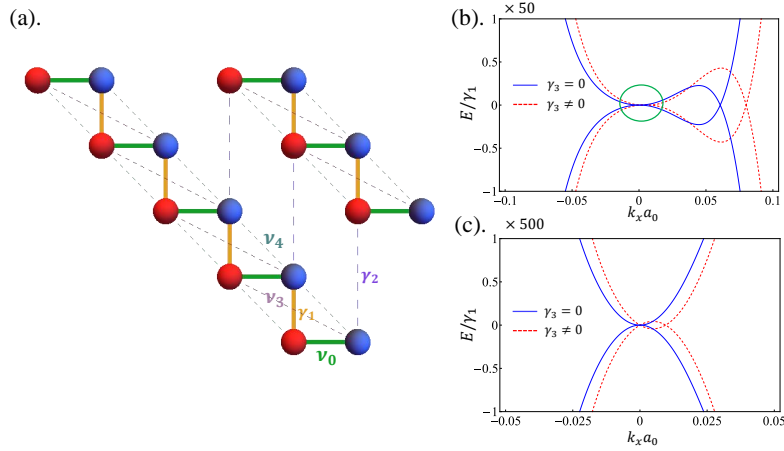


FIG. S1. (a). Side view of the rhombohedral pentalayer graphene (RPG), the blue and red atoms represent the A and B sublattices, respectively. The hopping parameters are indicated by different colors: $\gamma_0 = 3160 \text{ meV}$, $\gamma_1 = 390 \text{ meV}$, $\gamma_2 = -20 \text{ meV}$, and $\gamma_4 = 44 \text{ meV}$. Here, the displacement field and staggered layer orders are set to zero: $\Delta = 0$, and $m = 0$. (b). The band structure for the low-energy effective model with and without $\gamma_3 = 315 \text{ meV}$, which are shown by red dashed and blue solid lines, respectively. (c). Enlarged view of the band structure for the region marked by the green circle in (b).

displacement field can be expressed as:

$$H_\Delta = \Delta \text{Diag}(D_1, D_2, \dots, D_N), \quad (\text{S4})$$

where $D_l = \begin{pmatrix} 1 - \frac{2(l-1)}{N-1} & 0 \\ 0 & 1 - \frac{2(l-1)}{N-1} \end{pmatrix}$ (for $l = 1, 2, \dots, N$), and Δ is the amplitude of this interlayer potential.

Then, the effective two-band Hamiltonian under the basis (A_1, B_N) can be obtained by performing perturbation theory. Near K and K' valleys, due to the relation: $\gamma_1, |v_0\xi_{\mathbf{k}}| \gg |v_3\xi_{\mathbf{k}}|, |v_4\xi_{\mathbf{k}}|$, we can simplify the Hamiltonian by setting $\gamma_3 = 0$ and $\gamma_4 = 0$ in the result of the perturbation theory. Therefore, the Hamiltonian can be written as:

$$H = \begin{pmatrix} M_{N,eff}(k) & X_N(\mathbf{k}) \\ X_N^\dagger(\mathbf{k}) & -M_{N,eff}(k) \end{pmatrix}, \quad (\text{S5})$$

where the effective mass term $M_{N,eff}(k)$ is momentum-dependent and can be expressed as:

$$M_{N,eff}(k) = (m + \Delta) - \frac{((N-1)m - (N-3)\Delta)v_0^2 a_0^2 k^2}{(N-1)\gamma_1^2}. \quad (\text{S6})$$

In this effective mass (Eq. (S6)), m is the amplitude of the staggered layer order, Δ is the amplitude of the interlayer potential induced by the displacement field, a_0 is the lattice constant of the graphene, and $k^2 = \xi_{\mathbf{k}}\xi_{\mathbf{k}}^\dagger = |k_x + ik_y|^2$. As discussed in the main text, the combination of trigonal warping and the momentum dependence of the effective mass is responsible for the appearance of additional quantum anomalous Hall (QAH) states with Chern number $C \neq \pm N, \pm 2N$ in rhombohedral N -layer graphene. The effective hopping term $X_N(\mathbf{k})$ for two-band model is written as [50]:

$$X_N(\mathbf{k}) = \sum_{\{n_1, n_2\}} \frac{(n_1 + n_2)!}{n_1! n_2!} \frac{1}{(-\gamma_1)^{n_1 + n_2 - 1}} (v_0 \xi_{\mathbf{k}})^{n_1} \left(\frac{\gamma_2}{2}\right)^{n_2}, \quad (\text{S7})$$

where n_1 and n_2 are non-negative integers, and they satisfy $n_1 + 3n_2 = N$.

In rhombohedral pentalayer graphene, the band structure of the low-energy effective model under different displacement fields and a fixed staggered layer order is shown in Fig.2 of the main text. As the displacement field increases, the effective mass term for the three “leg” Dirac cones first changes sign at $\Delta = -m_l < -m$ (with $m < 0$), resulting in a topological phase transition with a change in the Chern number of ± 3 . As the displacement field continues to increase, the effective mass for the central band-touching point (quadratic touching) also changes sign at $\Delta = -m$, leading to a second topological phase transition with a change in the total Chern number of ± 2 .

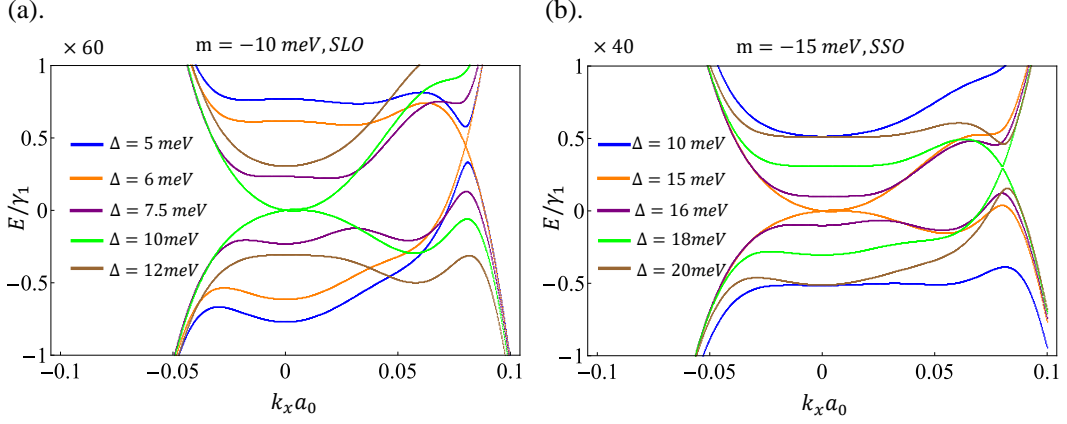


FIG. S2. (a). The evolution of the band structure for a fixed staggered layer order (SLO) $m = -10\text{meV}$ with increasing Δ . (b). The evolution of the band structure for a fixed staggered sublattice order (SSO) $m = -15\text{meV}$ with increasing Δ . Other parameters in (a) and (b) are: $v_0 = \frac{\sqrt{3}}{2} \times 3160\text{meV}$, $\gamma_1 = 390\text{meV}$, $\gamma_2 = -20\text{meV}$, $v_3 = \frac{\sqrt{3}}{2} \times 315\text{meV}$, and $v_4 = \frac{\sqrt{3}}{2} \times 40\text{meV}$.

B. The band structure and topological phase transition for the full Hamiltonian of RPG

In this section, to make the analysis more practical, we calculate the band structure of RPG using the full Hamiltonian shown in Eq. (S2) instead of the low-energy effective model, accounting for the staggered layer or sublattice order (SLO or SSO) and displacement field. The evolution of the bands with increasing displacement field for a fixed SLO and SSO, are shown in Fig. S2 (a) and (b), respectively. Although the band structure differs from the low-energy two-band model, the two-step topological phase transition behavior remains unchanged. Therefore, we can conclude that the low-energy two-band model can capture the key physical mechanism underlying the QAH states in RPG.

C. The effect of trigonal warping term γ_3 in rhombohedral pentalayer graphene

In this section, we discuss the effect of the trigonal warping term γ_3 on the low-energy effective model for rhombohedral pentalayer graphene (RPG). By using the perturbation theory mentioned in Sec. A, the two-band effective Hamiltonian for RPG can be written as:

$$H = \begin{pmatrix} M_{5,eff,2}(k) & X_{5,2}(\mathbf{k}) \\ X_{5,2}^\dagger(\mathbf{k}) & -M_{5,eff,2}(k) \end{pmatrix}, \quad (\text{S8})$$

where the effective mass term is:

$$M_{5,eff,2}(k) = (m + \Delta) - \frac{(2m - \Delta)v_0^2 k^2}{2\gamma_1^2}, \quad (\text{S9})$$

and the effective hopping $X_{5,2}(\mathbf{k})$ is:

$$X_{5,2}(\mathbf{k}) = \frac{v_0^5}{\gamma_1^4} (\xi_{\mathbf{k}}^\dagger)^5 - \frac{4v_0^3 v_3}{\gamma_1^3} (\xi_{\mathbf{k}}^\dagger)^3 (\xi_{\mathbf{k}}) + \frac{3v_0^2}{\gamma_1^2} (\xi_{\mathbf{k}}^\dagger)^2 \left(\frac{\gamma_2}{2}\right) + \frac{3v_0 v_3^2}{\gamma_1^2} (\xi_{\mathbf{k}}^\dagger) (\xi_{\mathbf{k}})^2 - \frac{2v_3}{\gamma_1} (\xi_{\mathbf{k}}^\dagger) \left(\frac{\gamma_2}{2}\right). \quad (\text{S10})$$

The low-energy bands near the K valley for RPG without and with γ_3 are shown in Fig. S1 (b) (and (c)). From these figures, we can conclude that the γ_3 -trigonal warping term induces further splitting of the central touching point. However, while this splitting transforms the quadratic band-touching at the K point into a central Dirac cone and three “leg” Dirac cones located at and around the K point, the momentum amplitude for the three “leg” Dirac cones remains very small due to the condition $v_0 \gg v_3$. Consequently, the condition for mass inversion in the central Dirac cone, $\Delta = -m$, is very close to the condition for mass inversion in the “leg” Dirac cones, $D = \frac{2\lambda-1}{1+\lambda}m$, where $\lambda = \frac{v_0^2 a_0^2 k^2}{2\gamma_1^2} \ll 1$. This proximity results in the same phase diagram as in the case of $\gamma_3 = 0$ when the displacement field increases at a fixed staggered layer order.

SUPPLEMENTAL MATERIAL NOTE 2: BERNAL MULTILAYER GRAPHENE

D. low-energy effective model for Bernal multilayer graphene

In this section, we derive the low-energy effective model for Bernal graphene with an even number of layers. The Hamiltonian for Bernal multilayer graphene (BMG) in the basis $\psi = (A_1, B_1, A_2, B_2, \dots, A_N, B_N)$ is written as:

$$H = \begin{pmatrix} H_0 & V & W & & & \\ V^\dagger & H'_0 & V^\dagger & W' & & \\ W & V & H_0 & V & W & \\ & W' & V^\dagger & H'_0 & V^\dagger & W' \\ & & & \ddots & \ddots & \ddots \\ & & & & & \ddots \end{pmatrix}, \quad (\text{S11})$$

where the intralayer hopping is expressed by $H_0 = \begin{pmatrix} 0 & v_0 \xi_{\mathbf{k}}^\dagger \\ v_0 \xi_{\mathbf{k}} & \delta \end{pmatrix}$, and $H'_0 = \begin{pmatrix} \delta & v_0 \xi_{\mathbf{k}}^\dagger \\ v_0 \xi_{\mathbf{k}} & 0 \end{pmatrix}$. In these equations, $\xi_{\mathbf{k}} = \zeta k_x + i k_y$ ($\zeta = \pm 1$ representing the K and K' valley, respectively), and δ represent the on-site energy for the dimerized atoms. The nearest interlayer hopping is represented by $V = \begin{pmatrix} -v_4 \xi_{\mathbf{k}}^\dagger & v_3 \xi_{\mathbf{k}} \\ \gamma_1 & -v_4 \xi_{\mathbf{k}}^\dagger \end{pmatrix}$, and the next-nearest interlayer hoppings are written as $W = \begin{pmatrix} \gamma_2/2 & 0 \\ 0 & \gamma_5/2 \end{pmatrix}$ and $W' = \begin{pmatrix} \gamma_5/2 & 0 \\ 0 & \gamma_2/2 \end{pmatrix}$. The side view and hopping parameters are labeled in Fig. S3 (a) ($v_i = \sqrt{3}\gamma_i/2$, in this figure, the tetralayer graphene is shown as an example).

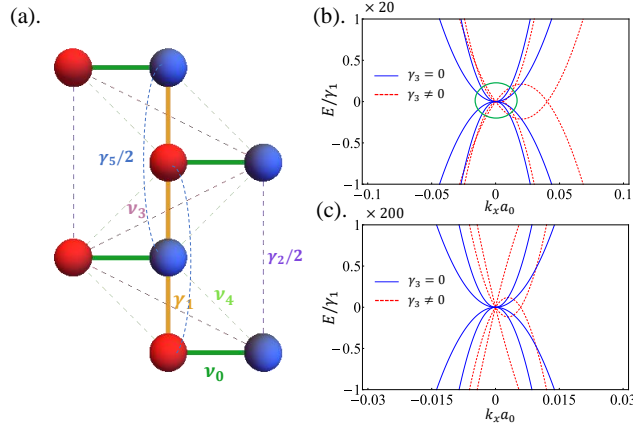


FIG. S3. (a). Side view of the Bernal tetralayer graphene (BTG), the blue and red atoms represent the A and B sublattices, respectively. The hopping parameters are indicated by different colors: $\gamma_0 = 3000 \text{ meV}$, $\gamma_1 = 400 \text{ meV}$, $\gamma_2 = -20 \text{ meV}$, $\gamma_4 = 40 \text{ meV}$, $\gamma_5 = 40 \text{ meV}$, $\delta = 40.8 \text{ meV}$. Here, the displacement field and staggered layer orders are set to zero: $\Delta = 0$, and $m = 0$. (b). The band structure for the low-energy effective model with and without $\gamma_3 = 300 \text{ meV}$, which are shown by red dashed and blue solid lines, respectively. (c). Enlarged view of the band structure for the region marked by the green circle in (b).

For N -layer BMG, as discussed in Ref.[71], we can decompose the Hamiltonian into a nearly block-diagonal form by using a unitary transformation. For $N \in \text{Even}$, the new basis is constructed by combining the old basis as follows:

$$\phi^{\text{new}} = (\phi_1^{A,\text{odd}}, \phi_1^{B,\text{odd}}, \phi_1^{A,\text{even}}, \phi_1^{B,\text{even}}, \dots, \phi_\alpha^{A,\text{odd}}, \phi_\alpha^{B,\text{odd}}, \phi_\alpha^{A,\text{even}}, \phi_\alpha^{B,\text{even}}, \dots, \phi_{N-1}^{A,\text{odd}}, \phi_{N-1}^{B,\text{odd}}, \phi_{N-1}^{A,\text{even}}, \phi_{N-1}^{B,\text{even}}), \quad (\text{S12})$$

where $\phi_\alpha^{X,\text{odd}} = \sum_{j=1}^N f_\alpha(j) X_j$, $\phi_\alpha^{X,\text{even}} = \sum_{j=1}^N g_\alpha(j) X_j$, and $\alpha = 1, 3, 5, \dots, N-1$. In these equations, $X = A$ or B , j labels the layers, $f_\alpha(j) = \sqrt{\frac{1}{N+1}} (1 - (-1)^j) \sin(\kappa_\alpha j)$, and $g_\alpha(j) = \sqrt{\frac{1}{N+1}} (1 + (-1)^j) \sin(\kappa_\alpha j)$, where $\kappa_\alpha = \frac{\pi}{2} - \frac{\alpha\pi}{2(N+1)}$. In addition, during the decomposition, we consider the staggered layer order given in Eq.(S3) and the interlayer potential induced by the displacement field, as shown in Eq.(S4). After decomposition, the resulting Hamiltonian can be interpreted as $N/2$ mutually coupled bilayer graphenes. For each bilayer graphene, the low-energy bands can be obtained by projecting the Hamiltonian onto the basis composed of non-dimerized ‘‘atoms’’:

$$\phi^{\text{new,low}} = (\phi_1^{A,\text{odd}}, \phi_1^{B,\text{even}}, \dots, \phi_\alpha^{A,\text{odd}}, \phi_\alpha^{B,\text{even}}, \dots, \phi_{N-1}^{A,\text{odd}}, \phi_{N-1}^{B,\text{even}}). \quad (\text{S13})$$

Therefore, by using the condition $\gamma_0, \gamma_1, \gamma_3 \gg |\gamma_2|, \gamma_4, \gamma_5, \delta$, the low-energy effective model for N -layer BMG can be written as:

$$H = \begin{pmatrix} h_{eff}(\lambda_1) + h_\Delta(s_{1,1}, t_{1,1}) & h_c(s_{1,3}, t_{1,3}) & h_c(s_{1,5}, t_{1,5}) & \dots \\ h_c(s_{1,3}, t_{1,3}) & h_{eff}(\lambda_3) + h_\Delta(s_{3,3}, t_{3,3}) & h_c(s_{3,5}, t_{3,5}) & \dots \\ h_c(s_{1,5}, t_{1,5}) & h_c(s_{3,5}, t_{3,5}) & h_{eff}(\lambda_5) + h_\Delta(s_{5,5}, t_{5,5}) & \dots \\ \vdots & \vdots & \vdots & \ddots \end{pmatrix}, \quad (\text{S14})$$

where $h_{eff}(\lambda) = \begin{pmatrix} 0 & \lambda v_3 \xi_{\mathbf{k}} - \frac{1}{\lambda \gamma_1} v_0^2 (\xi_{\mathbf{k}}^\dagger)^2 \\ \lambda v_3 \xi_{\mathbf{k}}^\dagger - \frac{1}{\lambda \gamma_1} v_0^2 (\xi_{\mathbf{k}})^2 & 0 \end{pmatrix}$, $h_\Delta(s, t) = \begin{pmatrix} s\Delta + m & 0 \\ 0 & t\Delta - m \end{pmatrix}$, and $h_c(s, t) = \begin{pmatrix} s\Delta & 0 \\ 0 & t\Delta \end{pmatrix}$. In these equations, $\lambda_\alpha = 2 \cos(\kappa_\alpha)$, $s_{\alpha,\beta} = \sum_{l'}^{N/2} f_\alpha(2l' - 1) f_\beta(2l' - 1) (1 - \frac{4l' - 4}{N - 1})$, and $t_{\alpha,\beta} = \sum_{l'}^{N/2} g_\alpha(2l') g_\beta(2l') (1 - \frac{4l' - 2}{N - 1})$.

For Bernal tetralayer graphene (BTG), the low-energy Hamiltonian can be written as:

$$H_{B-tetra} = \begin{pmatrix} h_{eff}(\lambda_1) + h_\Delta(s_{1,1}, t_{1,1}) & h_c(s_{1,3}, t_{1,3}) \\ h_c(s_{1,3}, t_{1,3}) & h_{eff}(\lambda_3) + h_\Delta(s_{3,3}, t_{3,3}) \end{pmatrix}, \quad (\text{S15})$$

where $\lambda_1 = (\sqrt{5} - 1)/2$, $\lambda_3 = (\sqrt{5} + 1)/2$, $s_{1,1} = -t_{1,1} = \frac{1}{15}(5 + 2\sqrt{5})$, $s_{3,3} = -t_{3,3} = \frac{1}{15}(5 - 2\sqrt{5})$, and $s_{1,3} = t_{1,3} = \frac{4}{3\sqrt{5}}$. The band structures for the low-energy effective model with and without $\gamma_3 = 300$ meV are shown in Fig. S3 (b) (and (c)). Here, the interlayer potential Δ induced by the displacement field and the staggered layer order m are set to zero.

E. The band structure and topological phase transition for the full model of the Bernal tetralayer graphene

In this section, we calculate the band structure for the full model of Bernal tetralayer graphene (Eq. (S11)) for the case where $N = 4$, and investigate the topological phase transition that occurs as the displacement field increases in the presence of staggered layer orders (Eq. (S3)). From the results shown in Fig. S4, we can conclude that the QAH state with a total Chern number $C = 6$ persists.

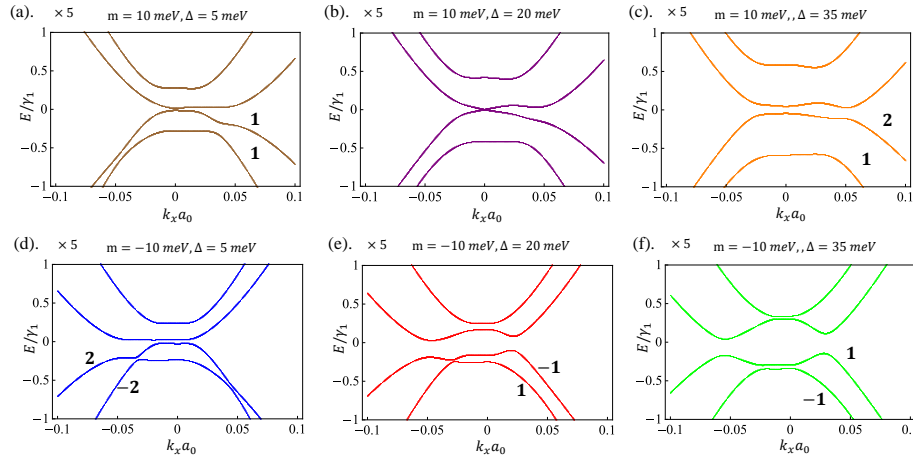


FIG. S4. (a), (b), (c). The band structure for the full model of Bernal tetralayer graphene under the increasing displacement field in the presence of the staggered layer orders $m = 10$ meV in K valley. (d), (e), (f). The band structure for the full model of Bernal tetralayer graphene under the increasing displacement field in the presence of the staggered layer orders $m = -10$ meV in K' valley. The Chern number for each valence band is indicated near the respective band. The hopping parameters are: $v_0 = \frac{\sqrt{3}}{2} \times 3000$ meV, $\gamma_1 = 400$ meV, $\gamma_2 = -20$ meV, $v_3 = \frac{\sqrt{3}}{2} \times 300$ meV, $v_4 = \frac{\sqrt{3}}{2} \times 40$ meV, and $\gamma_5 = 40$ meV.